



Template-free synthesis of 2D porous ultrathin nonmetal-doped g-C₃N₄ nanosheets with highly efficient photocatalytic H₂ evolution from water under visible light



Xiaojie She, Liang Liu, Haiyan Ji, Zhao Mo, Yeping Li, Liying Huang, Daolin Du, Hui Xu*, Huaming Li*

School of the Environment and Safety Engineering, Institute for Energy Research, Jiangsu University, Zhenjiang 212013, PR China

ARTICLE INFO

Article history:

Received 24 September 2015
Received in revised form
21 December 2015
Accepted 29 December 2015
Available online 2 January 2016

Keywords:

g-C₃N₄
Chemical oxidation
Porous nanosheet
Photocatalysis
Hydrogen production

ABSTRACT

The novel two-dimensional (2D) porous ultrathin oxygen-doped g-C₃N₄ nanosheets (PUOCNs) were prepared. The comprehensive characterization methods were used to study morphology, microstructure, crystal structure, chemical states and photocatalytic performance of PUOCNs. 2D porous ultrathin structure and the introduction of oxygen are beneficial to the enhancement of the photocatalytic activity of PUOCNs. The average H₂ evolution rate of PUOCNs is ~189.3 μmol h⁻¹, which is ~5.2 times higher than that of the bulk g-C₃N₄ and the degradation efficiency of organic dye methyl orange (MO) is almost 71 times higher than that of the bulk g-C₃N₄. The enhanced photocatalytic activity is due to the more adsorption sites and more active sites, the enhanced redox ability and improved electron transport ability, which leads to less recombination and a more efficient separation of photogenerated electron and hole pairs. Through XPS VB and ESR analysis, the photocatalytic mechanism was also researched in detail.

© 2015 Elsevier B.V. All rights reserved.

1. Introduction

With the aggravation of energy dilemma and environmental issues, the photocatalysis technology has become one of the most promising technologies. About 40 years ago, Fujishima and Honda published the seminal paper on photocatalyzed water splitting of TiO₂ [1]. Therefore, the photocatalysis technology rapidly developed both in the directly photo-splitting water hydrogen production and the photocatalytic degradation of pollutants [2–7]. Especially, the hydrogen production through photocatalyzing water splitting has become one of the most exciting, sustainable and environmentally friendly technologies of producing renewable fuels. The semiconductor converts solar energy to chemical hydrogen energy from water, subsequently, chemical hydrogen energy can be used to form water [4]. This process known as “hydrogen economy” is hopeful to replace the traditional combustion of fossil fuels [4]. Hence, all kinds of semiconductor photocatalysts (Rh-doped SrTiO₃, TaON, La-doped NaTaO₃ and so on) [4,8,9] were prepared. However, none of them could meet the needs of practical application for they are usually made up of the rare and expen-

sive elements or noble metals, which made their preparation very uneconomical [4]. And some of them are ultraviolet-light-drive photocatalysts. As it is known that ultraviolet only takes ~4% of the incoming solar energy and visible light is ~46% [10–12]. Thus the exploration of the visible-light-driven photocatalyst has been a focus.

Graphitic carbon nitride (g-C₃N₄) with a layer structure is a non-metallic polymeric organic semiconductor. The nontoxic g-C₃N₄ with visible light response, high thermal and chemical stability, appropriate band positions and other properties, has been widely researched for the photocatalytic water splitting and photocatalytic organic pollution degradation under visible light irradiation [2,7,13–16]. Nevertheless, the photocatalytic activity of the bulk g-C₃N₄ is very low due to the high recombination rate of photo-generated electron-hole pairs, low quantum efficiency, few active sites and adsorption sites etc., [7,17–19]. Thus, many strategies have been taken to improve the photocatalytic activity of the bulk g-C₃N₄, such as morphology control [13], preparation of novel nanostructures [20], chemical modification by foreign elements, band alignment by coupling with other semiconductor photocatalysts or some co-catalysts to improve the electron-hole separation [4,21–28].

It can be known that 2D materials have the large surface areas which can provide more active sites and more adsorption sites. 2D

* Corresponding authors. Fax: +86 511 88791708.

E-mail addresses: xh@ujs.edu.cn (H. Xu), lihm@ujs.edu.cn (H. Li).

structure is also beneficial to interface photoexcited charge transfer and 2D g-C₃N₄ can possess the quantum confinement effect [29,30]. In addition, the doping some heteroatoms (S, P, F and B) can change the bandgap of the bulk g-C₃N₄, which can improve the redox ability [31–34]. These methods have been proved to be able to effectively enhance photocatalytic performance of the bulk g-C₃N₄. Thus, if the morphology, intrinsic electronic structure and band positions of the bulk g-C₃N₄ can be modulated simultaneously, the photocatalytic performance of the bulk g-C₃N₄ may be greatly improved. Inspired by Hummers method used to prepare graphene oxide, if oxygen-containing functional groups can be introduced into g-C₃N₄, its performance should be fascinating. However, the structure of the bulk g-C₃N₄ is different from that of graphite. It has stronger covalent C–N bonds instead of C–C bands in each layer [35]. And the planar cohesion of the bulk g-C₃N₄ is mainly attributed to hydrogen bonding between strands of polymeric melon units with NH/NH₂ groups and not weak van der Waals force [30,36–38]. Thus, some methods, like Hummers method, are not suitable to prepare the 2D oxygen-doping g-C₃N₄ [36]. But, if 2D g-C₃N₄ can be prepared firstly, and then, it is oxidized, there will be a very good strategy for preparing the 2D oxygen-doping g-C₃N₄. However, the oxidants are multitudinous, such as HNO₃ [39], K₂Cr₂O₇ + H₂SO₄ [35,40,41], KMnO₄ + H₂SO₄ [42], HNO₃ + H₂SO₄ [42] and so on. The different oxidants have a great impact on the degree of oxidation. For example, the strong oxidant (KMnO₄ + H₂SO₄ used by Hummers method) can destroy the structure of g-C₃N₄ [36,37]. The single HNO₃ or HCl or H₂SO₄ is not capable of oxidizing g-C₃N₄, and it can only protonate it or smash it or exfoliate it, which is for the reason that the oxidizability of the single mineral acid is not enough to oxidate the bulk g-C₃N₄ [37,43]. The mixed acid (HNO₃ + H₂SO₄) has a stronger oxidizing ability than that of single mineral acid (HNO₃, H₂SO₄, HCl) and the oxidizing ability of the mixed acid (HNO₃ + H₂SO₄) is weaker than that of KMnO₄. Thus, the appropriate oxidizability of the mixed acid (HNO₃ + H₂SO₄) is not like that of the single mineral acid and Hummers method (protonate and smash g-C₃N₄ or destroy the structure of g-C₃N₄). Additionally, the synergistic effects of the strong dehydration property and oxidizing ability of H₂SO₄ and HNO₃ can also be good for oxidizing g-C₃N₄. Thus, the mixed acid (HNO₃ + H₂SO₄) can be more capable of oxidizing g-C₃N₄, making oxygen-containing functional groups bond with g-C₃N₄, instead of forming g-C₃N₄ particles or decomposing the structure of g-C₃N₄. Finally, the unique oxidant (HNO₃ + H₂SO₄) with a appropriate redox potential can be used to oxidize the bulk g-C₃N₄.

Herein, we demonstrated the preparation of 2D porous ultra-thin O-doped g-C₃N₄ nanosheets by the facile strategy (the calcined method and chemical oxidation method at room temperature). The prepared sample has a 2D porous ultrathin structure. The morphology, intrinsic electronic structure and band positions of the bulk g-C₃N₄ are modulated simultaneously. The formations of 2D porous nanosheets and oxygen-containing functional groups result in the superior photocatalytic performance towards H₂ evolution and organic dye methyl orange (MO) degradation under visible light irradiation.

2. Experimental

2.1. Reagents and chemicals

Melamine (>99.0%), Ethanol (99.7%), H₂SO₄ (95.0–98.0%) and HNO₃ (65–68%) were purchased from Sinopharm Chemical Reagent Co., Ltd., (China). Doubly distilled water was used throughout this work. All other reagents were of analytical reagent grade, without further purification.

2.2. Preparation of the samples

The bulk g-C₃N₄ was prepared using the method as in our previous report. Simply, the bulk g-C₃N₄ was prepared by directly heating melamine. 2 g melamine in a crucible with a cover was heated at 550 °C for 4 h and the heating rate of this condensation reaction was 2 °C/min. Then, the bulk g-C₃N₄ ground into powder was heated at 550 °C again. Therewith, 0.1 g of the heated sample was put into the flask, and 20 mL H₂SO₄ and 20 mL HNO₃ were added. The suspension was stirred magnetically for 5 h at room temperature. After that, the mixture was centrifuged at 13,000 rpm so that all residual acids could be removed. And the obtained sample was washed with distilled water until the solution's pH was 7. Finally, the obtained sample was the freeze-drying and was denoted as PUOCNs.

2.3. Photoelectrochemical measurement

The photocurrents of the samples were measured with an electrochemical analyzer (CHI660B, Chen Hua Instruments, Shanghai, China). In a standard three-electrode system, a platinum wire was employed as the counter electrode, indium tin oxide (ITO) glass was employed as the working electrode, and Ag/AgCl (saturated KCl solution) was employed as the reference electrode. 5 mg sam-

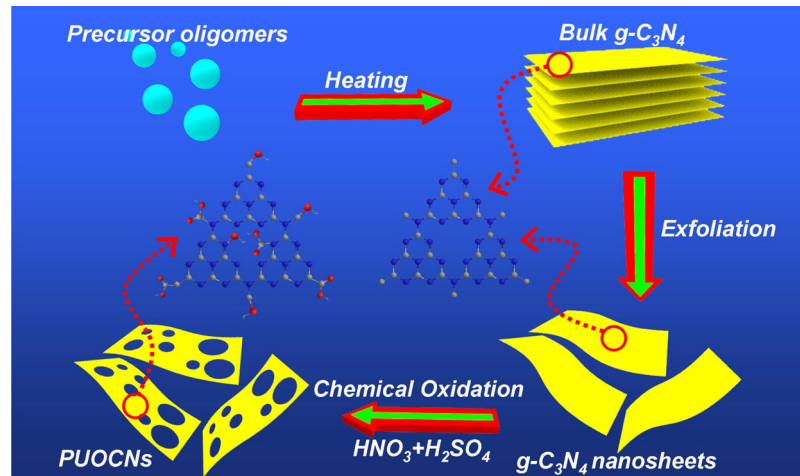


Fig. 1. Schematic illustration of preparing PUOCNs.

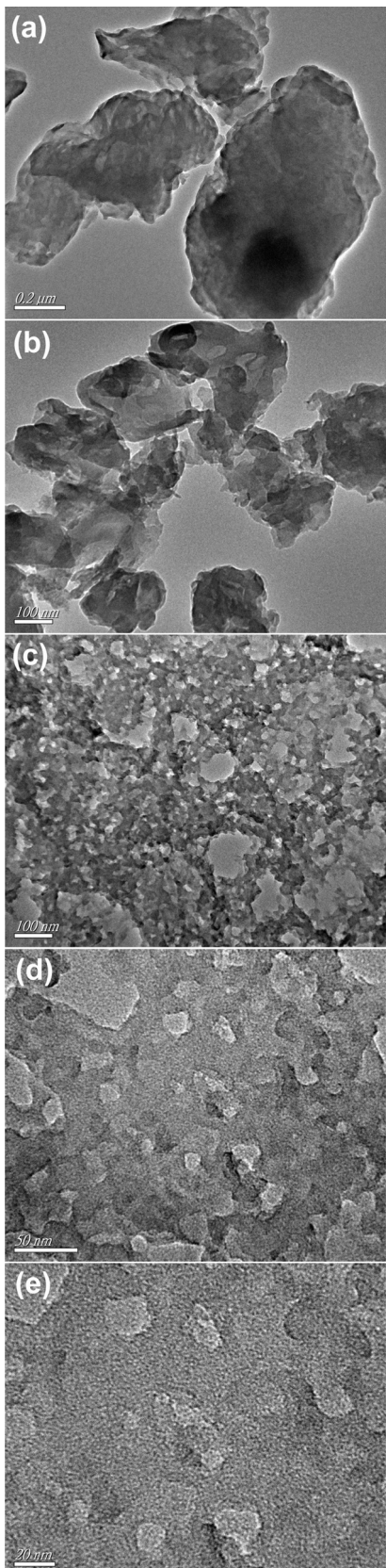


Fig. 2. Typical TEM images with different magnifications of the bulk $\text{g-C}_3\text{N}_4$ (a and b) and PUOCNs (c–e).

ple powder was dispersed ultrasonically in 0.5 mL of ethanol and 0.5 mL of Ethylene glycol. Then, 20 μL of the resulting colloidal dispersion (5 mg/mL) was drop-cast onto a piece of ITO with a fixed area of 0.5 cm^2 , and dried under an infrared lamp to form the sample-modified ITO electrode. All the photocurrent measurements were performed at a constant potential of -0.2 V (vs. SCE). Sodium nitrate solution (NaNO_3 , 0.1 M) was used as the supporting electrolyte for photocurrent measurements. A 500 W Xe arc lamp was utilized as the light source.

2.4. Photocatalytic activity

The photocatalytic hydrogen production reaction was carried out in an online photocatalytic hydrogen production system (LbSolar-3AG, PerfectLight, Beijing). 0.05 g of photocatalysts was added into aqueous solution (90 mL water and 10 mL hole sacrificial agent). Then, co-catalysts Pt nanoparticles were added by the in-situ photodeposition method and 3 wt.% (respect to Pt) $\text{H}_2\text{PtCl}_6 \cdot 6\text{H}_2\text{O}$ was added. Next, the solution was degassed and irradiated by a 300 W Xenon lamp (PLS-SXE 300C (BF), PerfectLight, Beijing) with an optical filter ($\lambda > 400 \text{ nm}$). The photocatalytic H_2 evolution rate was determined using an online gas chromatograph (GC D7900P, TCD detector, N_2 carrier, 5A molecular sieve column, Shanghai Fechcomp).

In addition, the MO with high photostability and water solubility was used as a model pollutant. In detail, 10 mg of the sample was added into 50 mL MO (10 mg/L) in a Pyrex photocatalytic reactor with a circulating water system to maintain a constant temperature (30°C). Prior to irradiation, the suspensions were magnetically stirred for 30 min in the dark to ensure that MO could reach the absorption–desorption equilibrium on the photocatalyst surface. At certain time intervals, 3 mL aliquots were sampled and centrifuged to remove the photocatalyst particles. Then the filtrates were analyzed by recording variations of the absorption band maximum (464 nm) in the UV-vis spectra of MO using a UV-vis spectrophotometer (UV-2450 Shimadzu). The air velocity was 2 L/min and the photocatalytic reaction was performed under a 300 W Xe lamp with a 400 nm cutoff filter.

2.5. Characterization

The transmission electron microscopy (TEM) images were recorded on a JEOL-JEM-2010 (JEOL, Japan) operated at 200 kV. The powder X-ray diffraction (XRD) patterns was recorded using a Bruker D8 diffractometer with $\text{Cu K}\alpha$ radiation ($\lambda = 1.5418 \text{ \AA}$) in the range of $2\theta = 10\text{--}80^\circ$. X-ray photoelectron spectroscopy (XPS) analysis was performed on an ESCALab MKII X-ray photoelectron spectrometer using $\text{Mg K}\alpha$ radiation. The Fourier transform infrared spectra (FT-IR) of the samples were recorded using a Nicolet Nexus 470 spectrometer. Ultraviolet visible (UV-vis) diffuse reflection spectra were measured using a UV-vis spectrophotometer (Shimadzu UV-2450, Japan) in the range of 200–800 nm. BaSO_4 was used as a reflectance standard material.

3. Results and discussion

3.1. Mechanism of the formation of PUOCNs

The synthetic strategy of PUOCNs is illustrated in Fig. 1. In this process, the calcination and the chemical oxidation methods have played a leading role. According to reports, the calcination contributes to the formation of two-dimensional (2D) structure and the chemical oxidation results in the porous structure [30,35,37]. At the same time, the chemical oxidation results in various oxygen-containing functional groups or makes some defect sites produce on $\text{g-C}_3\text{N}_4$, which may be very important to enhance photocatalytic

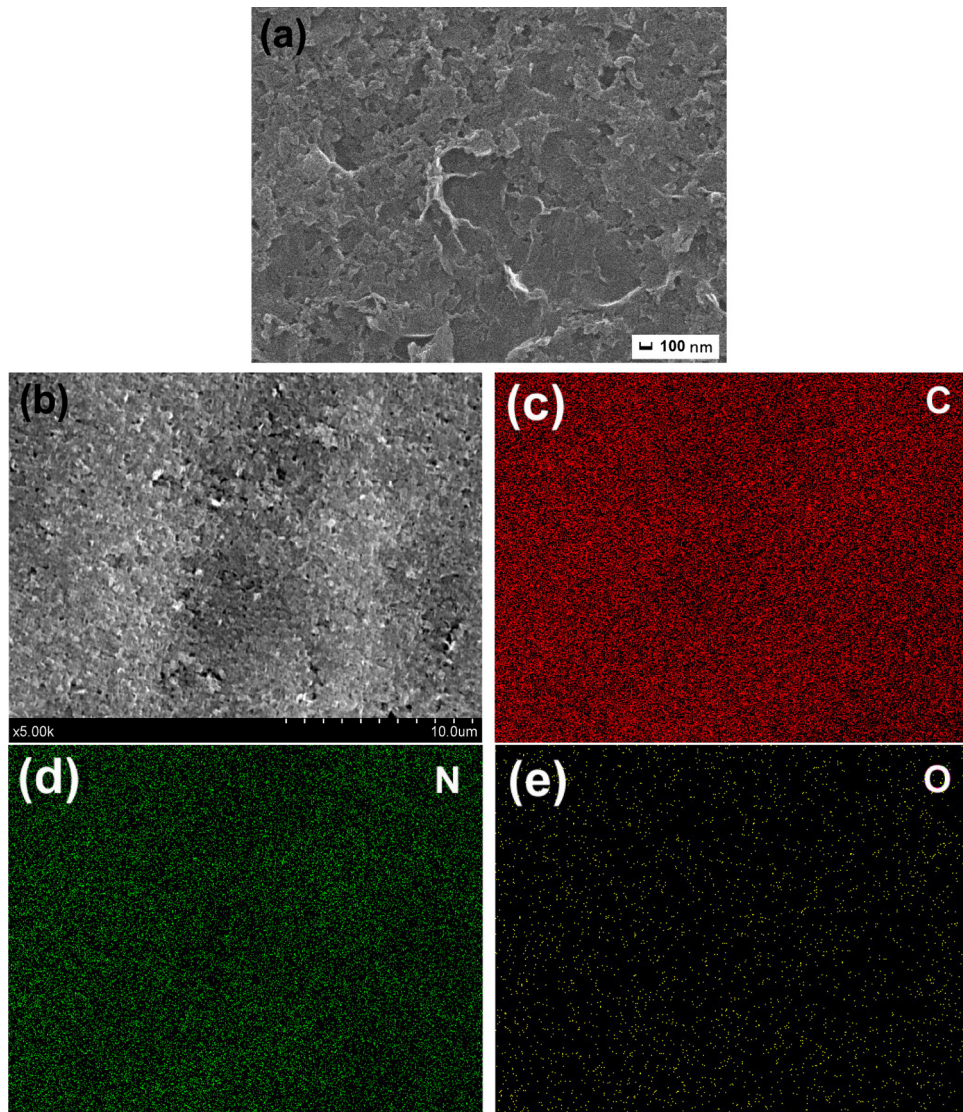


Fig. 3. SEM images of PUOCNs (a and b) and corresponding EDS elemental mapping (c–e) from b for C, N and O.

activity [35,44,45]. These oxygen-containing functional groups can also prevent the stacking of 2D materials [46]. It is worth noting that this unique structure was not found in the process of treating the bulk g-C₃N₄ or 2D g-C₃N₄ with common single mineral acids, such as HNO₃, HCl and H₂SO₄ [43,47,48]. Thus, it can be known that the mixed acid (H₂SO₄ and HNO₃) is very significant for preparing the porous structure.

During the process of adding the mixed acid, the rapid heating effect can contribute to the dispersion and chemical oxidation of the sample [35,48]. Then, the mixed acid can effectively corrode the surface of sample and produce hydroxyl groups. These hydroxyl groups can be further oxidized to form quinone groups or carboxy groups [35]. According to the results of this work, it is obvious that the oxidizability of the mixed acid (H₂SO₄ and HNO₃) is milder than KMnO₄. The redox potential of KMnO₄ (1.679 eV) is greater than that of H₂SO₄ (0.172 eV) and HNO₃ (0.934 eV) [35,49]. Thus, Hummers method is not suitable for preparing 2D g-C₃N₄ nanosheets and porous g-C₃N₄. Due to the synergistic effects caused by the strong dehydration property and oxidizing ability of H₂SO₄ and HNO₃, PUOCNs is prepared successfully, and in this process, 2D structure of the sample is still well-preserved. However, the ratio of the mixed acid is not researched in this work because the phe-

nomenon of oxidizing g-C₃N₄ to the porous structure may be more significant.

3.2. Morphology characterization

The morphologies of the bulk g-C₃N₄ and PUOCNs were investigated by TEM as shown in Fig. 2. The bulk g-C₃N₄ exhibits the irregular, thick and block characteristics, as shown in Fig. 2a and b. It is like the solid rocks and the size is within ~200–1000 nm in width. However, the structure of PUOCNs is different, as shown in Fig. 2c–e. PUOCNs is of the nanosheet structure and it has lots of non-uniform networks. This phenomenon of networks may be driven by the π–π stacking effect between the layers and hydrogen bonding interactions mediated by the oxygen-containing groups (–COOH, –OH, –C=O) [50]. From Fig. 2e, it can be known that PUOCNs is almost transparent, which indicates that PUOCNs is 2D porous ultrathin nanosheets. Obviously, compared with the bulk g-C₃N₄, the structure of PUOCNs has been changed. In addition, from the high-magnification TEM images (Fig. 2d and e), it is found that the pore-size is within ~5–100 nm. SEM images (Fig. 3a and b) also show that PUOCNs is of 2D nanosheet structure and possesses lots of non-uniform networks. Due to its ultrathin nature, some PUOCNs

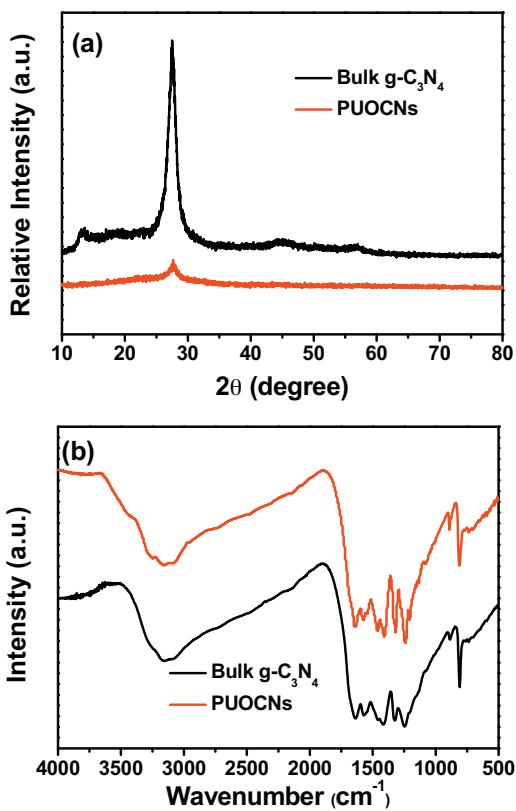


Fig. 4. (a) Powder XRD patterns and (b) FT-IR spectra of the bulk g-C₃N₄ and PUOCNs.

are curly. The elemental mappings reveal that C, N and O elements are homogeneously distributed throughout PUOCNs, as shown in Fig. 3c–e.

3.3. Crystal structure and chemical states

The crystal structure and chemical states of samples were researched by XRD, FT-IR, and XPS spectroscopy. From XRD (Fig. 4a), the XRD peaks (002) at ~27.28° and low-angle reflection peaks (100) at ~13.11° are due to the interlayer stacking reflection like that of the graphite and the in-plane repeated units, respectively [17,20]. The XRD pattern of PUOCNs is similar to that of the bulk g-C₃N₄, which indicates that the crystal structure of PUOCNs is not changed. Compared with the bulk g-C₃N₄, the intensity of the (002) peak of PUOCNs significantly decreases and the (100) peak almost disappears. This extent of reduction suggests that PUOCNs is of 2D structure [17,20,29,30]. And the peak (002) of PUOCNs is shifted from ~27.28° to 27.77°, showing a decreased gallery distance between the layers [20,30]. This feature can be due to the successful delamination of the bulk g-C₃N₄ and the introduction of oxygen heteroatoms [20]. Since the doped oxygen atoms on PUOCNs have higher electronegativity than the substituted nitrogen atoms [31], the interactions between the g-C₃N₄ layers can be strengthened by the stronger attraction resulted in the shortened interplanar distance.

From Fig. 4b, it can be known that the bulk g-C₃N₄ and PUOCNs show the typical FT-IR patterns of graphitic carbon nitride. The peaks at 807 cm⁻¹ are the characteristic breathing mode of the triazine ring system. The peaks at ~1242, 1322, 1412, 1563, and 1634 cm⁻¹ are typical stretching vibration modes of C=N and C—N heterocycles [17,20]. However C=O and C—O bonds are difficult to distinguish in PUOCNs by FT-IR. Because according to the work of Chen and Larkin, C—N, CC and C—O bonds have very similar force constants [31,32,35]. Hence, the typical stretching vibration modes

of C—N, C—C and C—O bonds can strongly couple, which can lead to their skeletal stretching vibrations in the common FT-IR regions [31]. Liao et al. reported that FT-IR peaks at ~1410 and 1220 cm⁻¹ are described to C—O in C—OH and C—O—C groups respectively [51]. Namely, the O-containing species in PUOCNs can be located in the same region of aromatic C—N stretching [31]. In addition, due to a small number of O atoms in PUOCNs, the C—O species are also difficult to clearly differentiate by FT-IR spectrometer. Hence, the low intensity peaks of C—O species in PUOCNs may be covered by aromatic C—N stretching in PUOCNs. In addition, the broad peak between 3600 and 3000 cm⁻¹ is caused by the N—H and O—H stretches [17,20,31].

The most direct evidence of oxygen doped in PUOCNs comes from XPS analysis. From Fig. 5a, there are only three elements (C, N, O) detected in samples. Obviously, the peak of O 1s in PUOCNs is stronger than that of the bulk g-C₃N₄, showing that there are a higher density of oxygen-containing species on PUOCNs surface. The O 1s core at ~532.58 eV of the bulk g-C₃N₄ is described to adsorbed water [31,52], as shown in Fig. 5b. There is no additional signal (about C—O or C=O) for the bulk g-C₃N₄. After acid treatment, three new O 1s peaks core at ~533.72 eV, 531.98 eV and 531.43 eV are detected, described to C—OH, C=O and N—C—O species [35,53,54], which means that oxygen in PUOCNs is present not simply as absorbed water but as various functional groups. The C 1s spectra of the bulk g-C₃N₄ and PUOCNs are shown in Fig. 5c. Obviously, PUOCNs shows a new-generated peak at ~288.96 eV, which can be assigned to the C—O bond [31,35]. It is obviously that O atoms can be bonded to sp²-hybridized carbon. The peaks at ~288.03 eV are corresponding to the C—N—C coordination [35]. Other peaks with low intensity at ~286.15 eV are related to the C—NH₂ [31,35]. The peaks located at ~284.69 eV are identified as carbon contamination [17]. Meanwhile, the N 1s spectra of samples are shown in Fig. 5d. Compared with the bulk g-C₃N₄, PUOCNs has a small binding energy shift of N 1s, which may be for the reason that the O atom substituting N atom has more electrons than N atom [31]. And these extra electrons can be delocalized among the big π bonds of PUOCNs, resulting in the shift of N 1s spectra of PUOCNs [35]. The peaks at ~401.08 eV, 400.04 eV and 398.47 eV can be attributed to terminal amino functions (C—N—H), sp³-hybridized nitrogen (N—(C)3) and sp²-hybridized nitrogen (C—N—C), respectively [17,20,29].

To identify the electronic structure and photoelectric property of PUOCNs, UV-vis diffuse reflectance spectroscopy (DRS) (Fig. 6a) and photoluminescence (PL) (Fig. 7a) spectra were used. UV-vis DRS spectra indicates that the absorption edge of PUOCNs displays a remarkable blue shift (from ~470 to 435 nm) in comparison with the bulk g-C₃N₄. The corresponding band gaps of the bulk g-C₃N₄ and PUOCNs are ~2.75 eV and 2.95 eV, respectively, as shown in Fig. 6b. The blue shift of the absorption edge of PUOCNs can be caused by the synergistic effect of the famous quantum confinement effect with the conduction and valence bands shifting in opposite directions, the electron-withdrawing groups from oxygen in sample and the color change from yellow of bulk g-C₃N₄ to white of PUOCNs [17,29,35], as shown in Fig. S1.

Fig. 7a is the PL spectra excited by 350 nm at room temperature. Obviously, the emission peak of PUOCNs is blue shifted by ~31 nm from ~470 to 439 nm, compared with the bulk g-C₃N₄. The blue shift of PL spectra is due to the famous quantum confinement effect [17]. In addition, PL spectrum of PUOCNs not only has a blue shift but also the intensity of the emission peak is significantly decreased, compared with the bulk g-C₃N₄. It indicates that the recombination of electron-hole pairs may be effectively inhibited on PUOCNs [31,35], which shows that PUOCNs can be the superior photocatalyst. Besides, Fig. 7b is the fluorescence decay curves of the samples. The measurements of the fluorescence lifetime are conducted to explore the charge transfer events of the

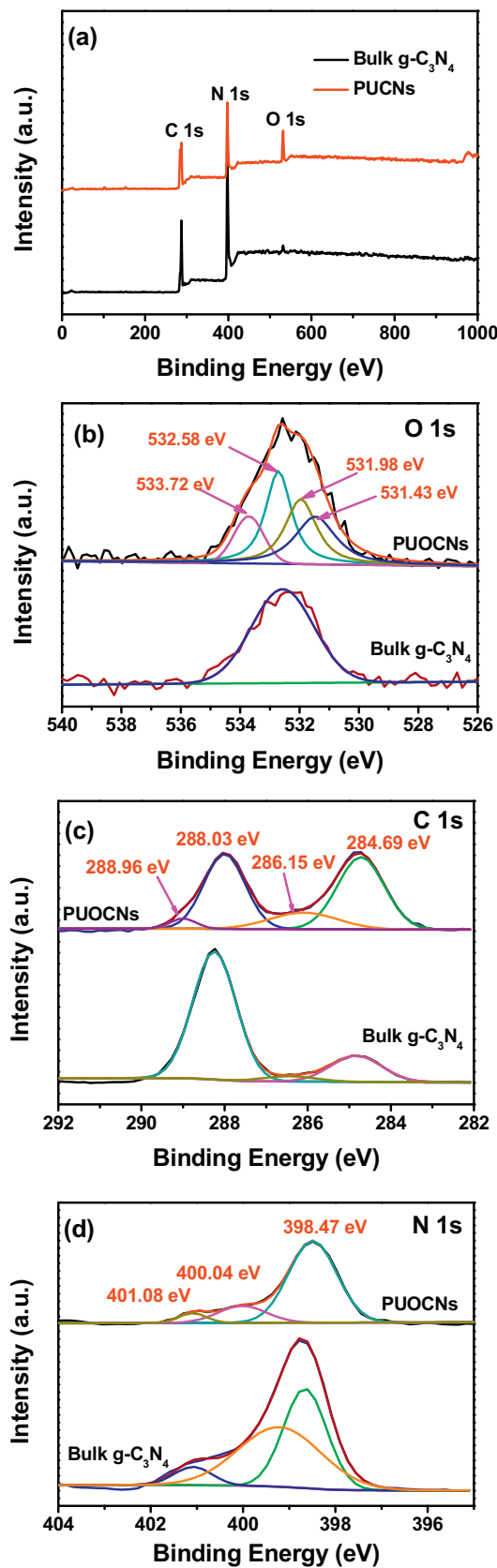


Fig. 5. (a) XPS survey spectra, high-resolution O 1s (b), C 1s (c) and N 1s (d) of the bulk g-C₃N₄ and PUOCNs.

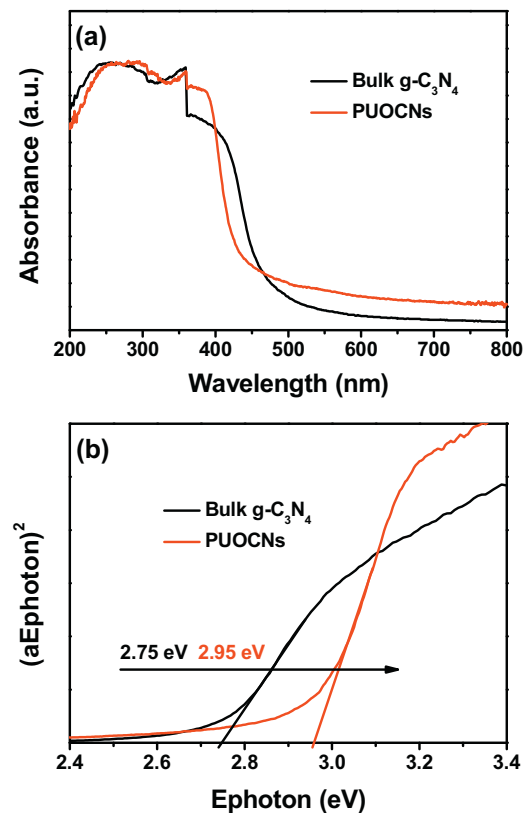


Fig. 6. (a) UV–vis absorption spectra and (b) estimated band gaps of the bulk g-C₃N₄ and PUOCNs.

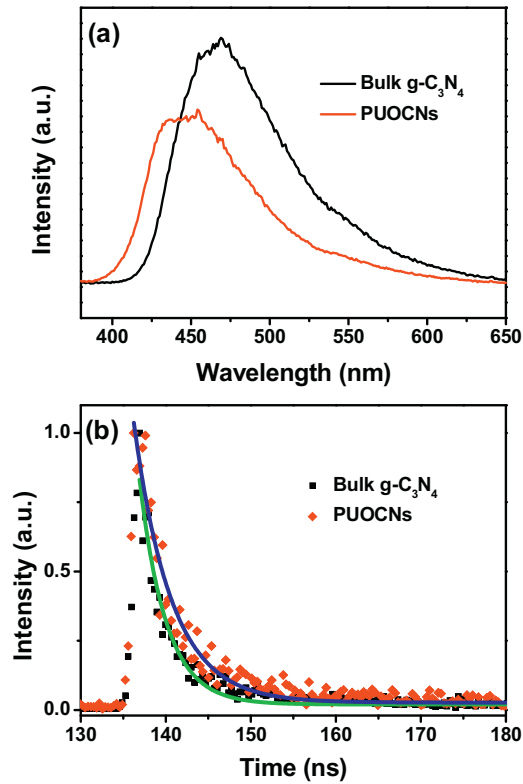


Fig. 7. (a) Photoluminescence spectra and (b) time-resolved fluorescence excited by the incident light of 337 nm at room temperature of the bulk g-C₃N₄ and PUOCNs.

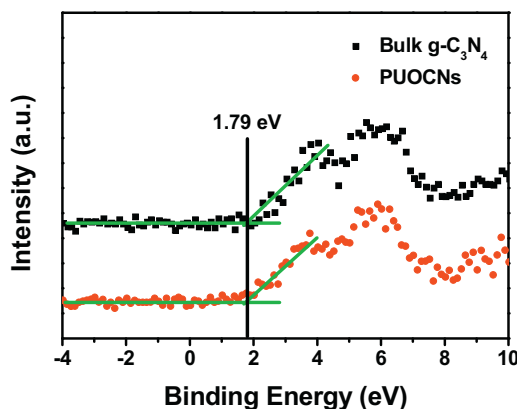


Fig. 8. The VB XPS spectra of the bulk $\text{g-C}_3\text{N}_4$ and PUOCNs.

samples. From the decay curves, the fluorescent intensities of the samples show deviation from the exponential decay. And the fluorescence lifetime of PUOCNs is increased, which shows that there may be a significant electronic interaction between the porous ultrathin graphitic carbon nitride and electrophilic groups (oxygen-containing functional groups). By the multi-exponential fitting, the radiative lifetime of the bulk $\text{g-C}_3\text{N}_4$ and PUOCNs is ~ 3.1 ns and 4.9 ns, respectively. Obviously, this result means that the radiative lifetime of the charge carriers of PUOCNs has been increased. Thus, it possesses better charge separation efficiency than the bulk $\text{g-C}_3\text{N}_4$ [30]. It is believed that the lifetime of charge carriers is associated with the improved electron transfer and electronic band structure changes induced by quantum confinement effect. The long radiative lifetime of electrons can play an important part in improving the probability of the participation of charge carriers in the photocatalytic reaction before recombination.

To further research the influence of oxygen-containing functional groups on positions of the conduction band (CB) and valence band (VB) of PUOCNs, the valence band X-ray photoelectron spectroscopy (VB XPS) was used. From Fig. 8, it can be known that PUOCNs has the same VB of ~ 1.79 eV as the bulk $\text{g-C}_3\text{N}_4$. Namely, it does not affect the VB of the bulk $\text{g-C}_3\text{N}_4$ with the introduction of oxygen atoms and 2D porous ultrathin structure. Because the potential of O 2p orbitals is lower than that of N 2p [31]. VB XPS shows that VB of PUOCNs relies on the N 2p orbitals. Combined with the UV-vis DRS result, it can be known that the CB of PUOCNs shifts from about -0.96 eV to -1.16 eV, which indicates that the redox ability of PUOCNs can be stronger than that of the bulk $\text{g-C}_3\text{N}_4$ [31].

From the above results, for the bulk $\text{g-C}_3\text{N}_4$, it can be believed that 2D porous ultrathin structure and the introduction of oxygen reduce the electron and hole recombination rate. Thus, the photogenerated charge separation and transfer performance were evaluated by a combined analysis of photocurrent and electrochemical impedance spectroscopy (EIS). Fig. 9a shows photocurrent-time curves of the samples. It can be observed that under visible light irradiation, the photocurrent response of PUOCNs increases with respect to the bulk $\text{g-C}_3\text{N}_4$, showing that PUOCNs has less recombination and a more efficient separation of photogenerated electron-hole pairs [17,20]. And the photocurrent is steady and recyclable. This can be described to the fact that 2D porous ultrathin structure is helpful to the transfer of photogenerated electrons in CB and electrophilic groups ($\text{C}-\text{O}$, $\text{C}=\text{O}$ and COOH) may inhibit the direct recombination of electrons and holes [20,35]. The experimental Nyquist impedance plots for the bulk $\text{g-C}_3\text{N}_4$ and PUOCNs are shown in Fig. 9b. The semicircle at high frequencies in the Nyquist diagrams is in accordance with the electron-transfer-limited process and the semicircle diameter is equivalent to the electron-transfer resistance (R_{et}) [14]. Obvi-

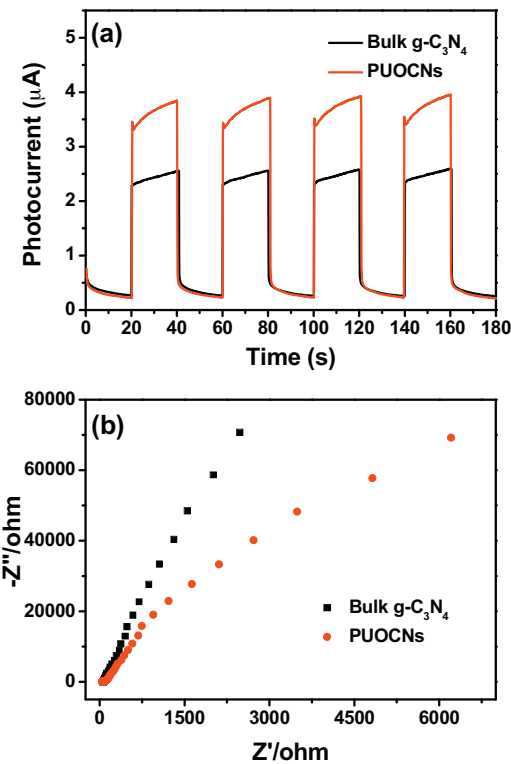


Fig. 9. (a) Photocurrent-time dependence under visible light irradiation and (b) EIS of the bulk $\text{g-C}_3\text{N}_4$ and PUOCNs in a 0.1 M NaNO_3 aqueous solution.

ously, PUOCNs has the smaller arc radius on EIS Nyquist plot than the bulk $\text{g-C}_3\text{N}_4$. This also means that PUOCNs has a more effective separation efficiency of photogenerated electron-hole pairs and a faster interfacial charge transfer [17]. The above characterization results of photocurrents and EIS analysis are consistent with the PL analysis, indicating that 2D porous ultrathin structure and the introduction of oxygen-containing functional groups are beneficial to improving separation efficiency of photogenerated electron-hole pairs.

3.4. Photocatalytic performance

The photocatalytic performance of the samples was evaluated with H_2 evolution from water and MO degradation under visible irradiation, as shown in Fig. 10. It can be seen that the bulk $\text{g-C}_3\text{N}_4$ has a low activity with a average H_2 evolution rate of ~ 36.3 $\mu\text{mol}/\text{h}$. However, the average H_2 evolution rate is ~ 189.3 $\mu\text{mol}/\text{h}$ for PUOCNs, which is ~ 5.2 times higher than that of the bulk $\text{g-C}_3\text{N}_4$. The stability of H_2 evolution on PUOCNs is determined by four cycling photocatalytic experiments under the same conditions. After the recycling runs, the photocatalytic activity of PUOCNs is sustained, which means PUOCNs is stable enough.

Fig. 10b shows the photocatalytic activity of samples for the degradation of MO under visible light irradiation. It can be known that MO self-degradation is almost negligible without photocatalyst under visible light irradiation. And the bulk $\text{g-C}_3\text{N}_4$ was almost inert for MO degradation under visible irradiation. However, after 3.5 h irradiation with visible light, $\sim 60.82\%$ MO is degraded by PUOCNs, and the photocatalytic degradation efficiency of MO by the bulk $\text{g-C}_3\text{N}_4$ is $\sim 0.96\%$. It is obvious that under the same conditions, the photocatalytic activity of PUOCNs is almost 71 times higher than that of the bulk $\text{g-C}_3\text{N}_4$. The above results clearly demonstrate the photocatalytic activity of PUOCNs has been significantly improved, compared with the bulk $\text{g-C}_3\text{N}_4$.

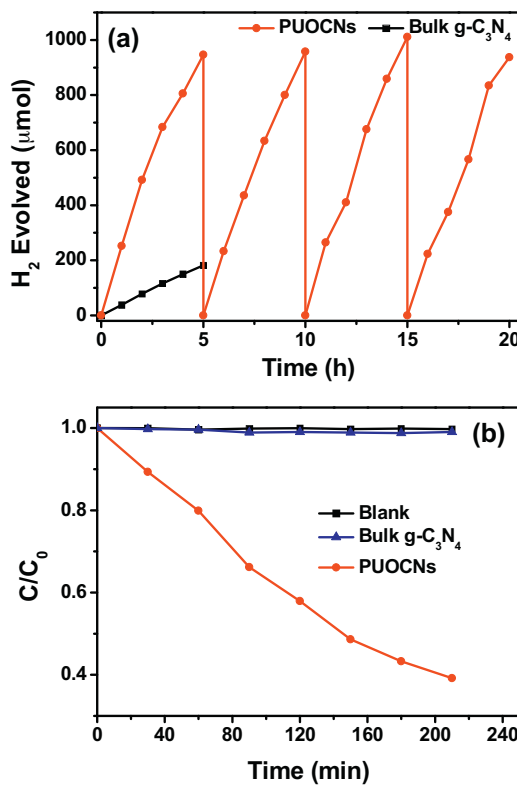
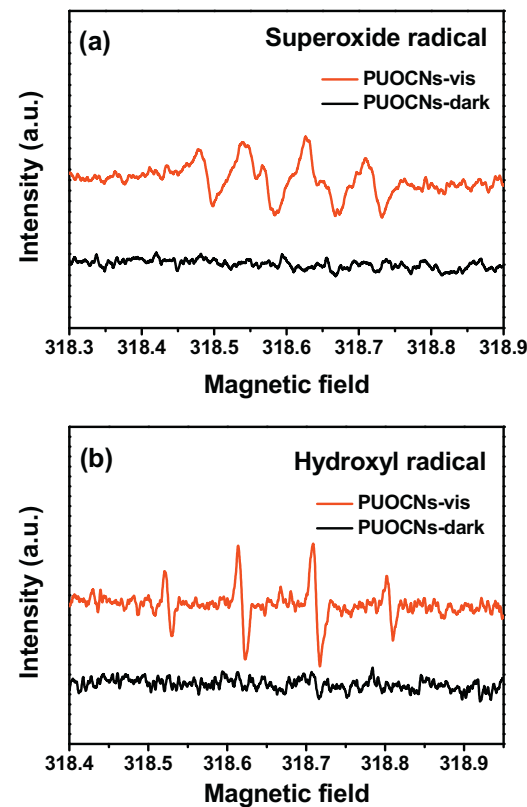


Fig. 10. (a) Timeline of photocatalytic H_2 evolution with 10 vol% triethanolamine aqueous solution, 3 wt% Pt as a co-catalyst and 0.05 g photocatalysts under visible light irradiation, and (b) the photocatalytic degradation of MO dye by the 0.02 g photocatalysts.

3.5. Mechanism for the photocatalysis

In most of the proposed mechanisms of the photocatalysis, it can be known when the photocatalyst is irradiated by light, the electrons and holes can be produced in CB and VB. No doubt the holes have the ability of oxidation and can also oxidate H_2O/OH^- into $\cdot OH$. But VB of PUOCNs is ~ 1.79 eV, indicating that the holes in VB can not oxidate H_2O/OH^- into $\cdot OH$ [14]. Thus, the holes can only oxidize some hole sacrificial reagents. Especially, when the adsorption of the photocatalysts is enough and the concentrations on photocatalyst surface is relatively high, the direct hole oxidation is easily initiated [14,16,31]. In addition, the electrons with the reducibility can make reduction reactions proceed, and also can combine with O_2 in the solution to form O_2^- with oxidability. Then O_2^- can combine with electron and H^+ to form $\cdot OH$ ($O_2 + e^- \rightarrow O_2^-$, $O_2^- + e^- + 2H^+ \rightarrow H_2O_2$, $H_2O_2 + e^- \rightarrow \cdot OH + OH^-$) [14,16,55–57]. To verify the active oxygen radicals of PUOCNs in the process of photocatalysis, the electrom spin resonance (ESR) signals of radicals spin-trapped by 5,5-dimethyl-1-pyrroline-N-oxide (DMPO) were recorded during photocatalytic degradation process, as shown in Fig. 11. Obviously, when the visible light is on, the characteristic signals of the DMPO- O_2^- (Fig. 11a) and DMPO- $\cdot OH$ (Fig. 11b) were observed, compared with PUOCNs for 8 min in dark. Hence, it can be known that the O_2^- and $\cdot OH$ can play a very significant role in photodegradation process.

The photoexcitation primarily relies on the bandgap structure of the semiconductor. The larger band gap (~ 0.20 eV) of PUOCNs can improve the conduction ability of photogenerated electrons, which is caused by the quantum confinement effect of PUOCNs. As is known, the redox ability of semiconductors is determinated by the potentials of VB and CB. From XPS VB and DRS, it can be found that the negative shift of CB of PUOCNs can make the electron



more reductive, and the VB is not changed, compared with the bulk $\text{g-C}_3\text{N}_4$.

Additionally, it can be known that the large BET specific surface area is very significant for enhancing photocatalytic activity. From Fig. S3 (the N_2 adsorption–desorption isotherm), it can be found that the specific surface area of the bulk $\text{g-C}_3\text{N}_4$ and PUOCNs is ~ 5.38 and $109.30 \text{ m}^2/\text{g}$, respectively. Obviously, the specific surface area of PUOCNs is improved a lot, which is ~ 20 times higher than that of the bulk $\text{g-C}_3\text{N}_4$. The huge specific surface area of PUOCNs can not only supply more active sites with adequate quality, but also offered more adsorption sites, which is significant for the photocatalytic activity.

According to the above results, the proposed mechanism for photocatalysis from PUOCNs is shown in Fig. 12. When PUOCNs is irradiated by visible light, photo-generated electrons and holes are produced at CB and VB. Normally, some electrons can recombine with holes inside the material (volume recombination), some can recombine with splices on surface (surface recombination), and the other can participate in photocatalytic reaction [10]. However, the high recombination rate of photoexcited electrons and holes results in the low photocatalytic activity of the bulk $\text{g-C}_3\text{N}_4$. But for PUOCNs, 2D porous ultrathin structure not only contributes to the conduction of photoexcited charge carriers but also can provide more adsorption sites and more active sites. In addition, the increased bandgap leads to more photoexcited electrons which can directly participate in hydrogen production (combine with H^+ to form H_2) or combine with O_2 to form O_2^- and O_2^- can also combine with electron and H^+ to form $\cdot OH$. For hydrogen production, holes can directly oxidate sacrificial reagents and Pt as a cocatalyst can make electrons transfer to the surface of PUOCNs and participate in reduction reaction to prepare H_2 . Thus, the reduction reaction of H^+ by electrons and the oxidation reaction of sacrificial reagents by holes can proceed. Besides, the generated O_2^- and $\cdot OH$

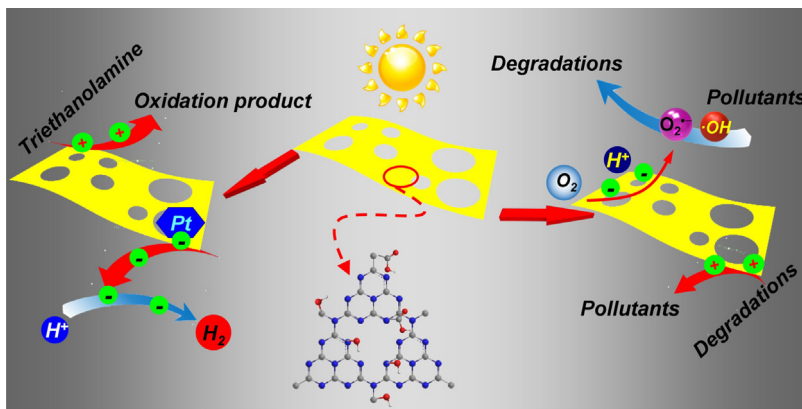


Fig. 12. Schematic illustration of proposed mechanism for the photocatalytic H_2 evolution and the degradation of the pollutant.

can also oxidize MO in photocatalytic degradation. Obviously, 2D porous ultrathin structure and oxygen doping all play significant roles in the photocatalysis process.

4. Conclusions

Finally, oxygen-doped $g\text{-C}_3\text{N}_4$ (PUOCNs) with 2D porous ultrathin structure was prepared successfully. PUOCNs shows outstanding photocatalytic performance for hydrogen production from water and degradation of the organic pollutant under visible light irradiation. The significantly enhanced photocatalytic activity is described to the synergistic effects of 2D porous ultrathin structure, the introduction of the electrophilic groups ($\text{C}=\text{O}$, $\text{C}=\text{O}$ and COOH) and increased bandgap, which not only inhibits electron-hole recombination probability but also improves redox ability of PUOCNs. Such modifications of morphology structure, intrinsic electronic structure and band positions consequently contribute to improving photocatalytic activity of PUOCNs. This work can provide a inspiration in modulating the physicochemical properties and the electronic structure of the photocatalysts or other materials.

Acknowledgments

The authors genuinely appreciate the financial support of this work from the National Nature Science Foundation of China. The authors genuinely appreciate the financial support of this work by the National Nature Science Foundation of China (21476097, 21476098, 21407065 and 21406094), the Natural Science Foundation of Jiangsu Province (BK20131207, BK2012717 and BK20140533).

Appendix A. Supplementary data

Supplementary data associated with this article can be found, in the online version, at <http://dx.doi.org/10.1016/j.apcatb.2015.12.046>.

References

- [1] A. Fujishima, K. Honda, *Nature* 238 (1972) 37–38.
- [2] X. Wang, K. Maeda, A. Thomas, K. Takanabe, G. Xin, J. Carlsson, K. Domen, M. Antonietti, *Nat. Mater.* 8 (2009) 76–80.
- [3] S. Cao, J. Low, J. Yu, M. Jaroniec, *Adv. Mater.* 27 (2015) 2150–2176.
- [4] V. Lau, M. Mesch, V. Duppel, V. Blum, J. Senker, B. Lotsch, *J. Am. Chem. Soc.* 137 (2015) 1064–1072.
- [5] C. Liu, J. Tang, H. Chen, B. Liu, P. Yang, *Nano Lett.* 13 (2013) 2989–2992.
- [6] B. Liu, C.H. Wu, J. Miao, P. Yang, *ACS Nano* 8 (2014) 11739–11744.
- [7] H. Xu, J. Yan, Y. Xu, Y. Song, H. Li, J. Xia, C. Huang, H. Wan, *Appl. Catal. B: Environ.* 128 (2013) 182–193.
- [8] A. Bard, *J. Photochem.* 10 (1979) 59–75.
- [9] H. Kato, M. Hori, R. Konda, Y. Shimodaira, A. Kudo, *Chem. Lett.* 33 (2004) 1348–1349.
- [10] J. Xu, X. Cao, *Chem. Eng. J.* 260 (2015) 642–648.
- [11] A. Kudo, Y. Miseki, *Chem. Soc. Rev.* 38 (2009) 253–278.
- [12] X. Chen, S. Shen, L. Guo, S. Mao, *Chem. Rev.* 110 (2010) 6503–6570.
- [13] J. Sun, J. Zhang, M. Zhang, M. Antonietti, X. Fu, X. Wang, *Nat. Commun.* 3 (2012) 1139.
- [14] F. Dong, Z. Wang, Y. Li, W. Ho, S. Lee, *Environ. Sci. Technol.* 48 (2014) 10345–10353.
- [15] Z. Zhao, Y. Sun, F. Dong, *Nanoscale* 7 (2015) 15–37.
- [16] Z. Wang, W. Guan, Y. Sun, F. Dong, Y. Zhou, W. Ho, *Nanoscale* 7 (2015) 2471–2479.
- [17] X. She, H. Xu, Y. Xu, J. Yan, J. Xia, L. Xu, Y. Song, Y. Jiang, Q. Zhang, H. Li, J. *Mater. Chem. A* 2 (2014) 2563–2570.
- [18] X. Wang, S. Blechert, M. Antonietti, *ACS Catal.* 2 (2012) 1596–1606.
- [19] S. Chu, Y. Wang, Y. Guo, J. Feng, C. Wang, W. Luo, X. Fan, Z. Zou, *ACS Catal.* 3 (2013) 912–919.
- [20] H. Xu, J. Yan, X. She, L. Xu, J. Xia, Y. Xu, Y. Song, L. Huang, H. Li, *Nanoscale* 6 (2014) 1406–1415.
- [21] Y. Di, X. Wang, A. Thomas, M. Antonietti, *ChemCatChem* 2 (2010) 834–838.
- [22] Z. Ding, X. Chen, M. Antonietti, X. Wang, *ChemSusChem* 4 (2011) 274–281.
- [23] Q. Xiang, J. Yu, M. Jaroniec, *J. Phys. Chem. C* 115 (2011) 7355–7363.
- [24] L. Ge, F. Zuo, J. Liu, Q. Ma, C. Wang, D. Sun, L. Bartels, P. Feng, *J. Phys. Chem. C* 116 (2012) 13708–13714.
- [25] H. Kang, S. Lim, D. Song, S. Park, *Int. J. Hydrog. Energy* 37 (2012) 11602–11610.
- [26] L. Sun, X. Zhao, C. Jia, Y. Zhou, X. Cheng, P. Li, L. Liu, W. Fan, *J. Mater. Chem.* 22 (2012) 23428–23438.
- [27] S. Cao, Y. Yuan, J. Barber, S. Loo, C. Xue, *Appl. Surf. Sci.* 319 (2014) 344–349.
- [28] J. Chen, S. Shen, P. Guo, M. Wang, P. Wu, X. Wang, L. Guo, *Appl. Catal. B: Environ.* 152 (2014) 335–341.
- [29] S. Yang, Y. Gong, J. Zhang, L. Zhan, L. Ma, Z. Fang, R. Vajtai, X. Wang, P. Ajayan, *Adv. Mater.* 25 (2013) 2452–2456.
- [30] P. Niu, L. Zhang, G. Liu, H. Cheng, *Adv. Funct. Mater.* 22 (2012) 4763–4770.
- [31] J. Li, B. Shen, Z. Hong, B. Lin, B. Gao, Y. Chen, *Chem. Commun.* 48 (2012) 12017–12019.
- [32] Y. Wang, J. Zhang, X. Wang, M. Antonietti, H. Li, *Angew. Chem. Int. Ed.* 49 (2010) 3356–3359.
- [33] Y. Zhang, T. Mori, J. Ye, M. Antonietti, *J. Am. Chem. Soc.* 132 (2010) 6294–6295.
- [34] G. Liu, P. Niu, C.H. Sun, S.C. Smith, Z.G. Chen, G.Q. Lu, H.M. Cheng, *J. Am. Chem. Soc.* 132 (2010) 11642–11648.
- [35] H. Li, B. Sun, L. Sui, D. Qian, M. Chen, *Phys. Chem. Chem. Phys.* 17 (2015) 3309–3315.
- [36] W. Wang, J. Yu, Z. Shen, D. Chan, T. Gu, *Chem. Commun.* 50 (2014) 10148–10150.
- [37] X. Zhang, H. Wang, H. Wang, Q. Zhang, J. Xie, Y. Tian, J. Wang, Y. Xie, *Adv. Mater.* 26 (2014) 4438–4443.
- [38] V. Lotsch, M. Doblinger, J. Sehnert, L. Seyfarth, J. Senker, O. Oeckler, W. Schnick, *Chem. Eur. J.* 13 (2007) 4969–4980.
- [39] S. Tsang, Y. Chen, P. Harris, M. Green, *Nature* 372 (1994) 159–162.
- [40] X. Chen, J. Xia, J. Peng, W. Li, S. Xie, *Compos. Sci. Technol.* 60 (2000) 301–306.
- [41] Z. Liu, X. Lin, J. Lee, W. Zhang, M. Han, L. Gan, *Langmuir* 18 (2002) 4054–4060.
- [42] H. Hiura, T. Ebbesen, K. Tanigaki, *Adv. Mater.* 7 (1995) 275–276.
- [43] Y. Xu, M. Xie, S. Huang, H. Xu, H. Ji, J. Xia, Y. Li, H. Li, *RSC Adv.* 5 (2015) 26281–26290.
- [44] J. Hong, S. Yin, Y. Pan, J. Han, T. Zhoua, R. Xu, *Nanoscale* 6 (2014) 14984–14990.
- [45] D. Tasis, N. Tagmatarchis, A. Bianco, M. Prato, *Chem. Rev.* 106 (2006) 1105–1136.
- [46] M. Zhao, Q. Zhang, J. Huang, G. Tian, J. Nie, H. Peng, F. Wei, *Nat. Commun.* 5 (2013) 3410.
- [47] Y. Zhang, A. Thomas, M. Antonietti, X. Wang, *J. Am. Chem. Soc.* 131 (2009) 50–51.
- [48] J. Xu, L. Zhang, R. Shi, Y. Zhu, *J. Mater. Chem. A* 1 (2013) 14766–14772.
- [49] C. Murthy, *University Chemistry*, New Age International (P) Ltd., 1995.

- [50] N. Medhekar, A. Ramasubramaniam, R. Ruoff, V. Shenoy, *ACS Nano* 4 (2010) 2300–2306.
- [51] G. Liao, S. Chen, X. Quan, H. Yu, H. Zhao, *J. Mater. Chem.* 22 (2012) 2721–2726.
- [52] C. Clayton, Y. Lu, *J. Electrochem. Soc.* 133 (1986) 2465–2473.
- [53] D. Yang, A. Velamakanni, G. Bozoklu, S. Park, M. Stoller, R. Piner, S. Stankovich, I. Jung, D. Field, C. Ventrice Jr., R. Ruoff, *Carbon* 47 (2009) 145–152.
- [54] F. Meng, X. Zhang, B. Xu, S. Yue, H. Guo, Y. Luo, *J. Mater. Chem.* 21 (2011) 18537–18539.
- [55] M. Hoffmann, S. Martin, W. Choi, D. Bahnemann, *Chem. Rev.* 95 (1995) 69–96.
- [56] Y. Cui, J. Huang, X. Fu, X.N. Wang, *Catal. Sci. Technol.* 2 (2012) 1396–1402.
- [57] S. Yan, Z. Li, Z. Zou, *Langmuir* 26 (2010) 3894–3901.